Journal of Materials Chemistry C

ROYAL SOCIETY OF CHEMISTRY

PAPER

View Article Online
View Journal

Cite this: DOI: 10.1039/d4tc03017f

A $Ca_3Sc_2Si_3O_{12}$:Ce^{3+},Cr^{3+},Li^+ phosphor-in-glass film for high-power laser-driven near-infrared lighting†

Ping Sui,‡[ab] Wei Zhang,‡[b] Hang Lin, *[ac] Bo Wang, [d] Pengfei Wang,[b] Yi Lin,[b] Ju Xu,[b] Yao Cheng [b] and Yuansheng Wang *[b]

Advanced laser-driven near-infrared (NIR) lighting demonstrates the evolution of invisible lighting/imaging technology towards long distances, high brightness and high resolution. In response to the shortage of laser-driven NIR phosphor color converters with desirable properties, herein, we designed and fabricated a $Ca_3Sc_2Si_3O_{12}$:Ce^{3+},Cr^{3+},Li^+ phosphor-in-glass film (PiGF) composite, which succeeded in realizing a blue-laser converted NIR optical output of 1.697 W. Elaborate experiments were carried out to optimize the preparation conditions and sample parameters. Microstructural and spectroscopic studies demonstrate an insignificant interfacial reaction during sintering and thus the retained luminescence performance of NIR phosphor powders. Upon laser-driven lighting, the luminescence saturation behavior was carefully examined in different excitation modes to gain insight into the saturation mechanism. It was found that Ce^{3+} ions become more susceptible to heat and Cr^{3+} ions suffer more from the incident high-density blue photons; correspondingly, thermal quenching/intensity quenching accounting for Ce^{3+} is 71%/29% and for Cr^{3+} is 26%/74% when luminescence saturation occurs. The demonstration experiment shows a better imaging effect and deeper penetration capability of the fabricated high-power laser-driven NIR illumination source than the conventional NIR LED, revealing its potential application in night vision and non-destructive analysis and identification.

Received 16th July 2024,
Accepted 15th August 2024

DOI: 10.1039/d4tc03017f

rsc.li/materials-c

1. Introduction

The spread of solid-state-lighting (SSL) technology has spawned a variety of new application scenarios that are not possible using the conventional lighting source. One important advancement is the development of near-infrared (NIR) SSL, applicable to active night vision imaging, food analysis, medical diagnostics, and material identification, whose compact size makes portable and hand-held NIR spectrometers possible.[1–6] The development of high-performance NIR light sources is at the cutting edge of SSL technology. At present, the mainstream NIR SSL product is based on light-emitting-diodes (LEDs), directly utilizing the NIR-emissive properties of the AlGaAs LED chip or convert the blue emission of the InGaN LED chip into broadband NIR emission *via* fluorescence conversion.[7–12]

Laser diode (LD) technology may bring a brighter future for SSL, which may lead to high brightness and energy savings.[13–15] LD-driven white light has promoted a billion-dollar-level industrial chain in the fields of laser lighting and displays. One major reason for using an LD to replace an LED is the ''efficiency droop'' of the LED, which results from the inevitable electron–hole Auger recombination under high driven current.[16–20] Likewise, the NIR LED is also plagued by the ''efficiency droop'': the limited input current imposes a restriction on the attainable NIR output power (whether for the NIR LED or phosphor-converted NIR LED, the output power based on single-chip design is always confined to tens of milliwatts).[21–24] The output could be improved by integrating multiple chips on board, but the cost, luminous efficiency and compactness would be compromised. The advantage of a high-power NIR lighting source is apparent: *e.g.*, when applied in active imaging, the increased NIR power will substantially improve the imaging contrast and working distance in dark vision;[25–27] and when applied in

[a] State Key Laboratory of Structural Chemistry, Fuzhou, Fujian, 350002, China. E-mail: lingh@fjirsm.ac.cn
[b] Key Laboratory of Optoelectronic Materials Chemistry and Physics, Fujian Institute of Research on the Structure of Matter, Chinese Academy of Sciences, Fuzhou, Fujian, 350002, China. E-mail: yswang@fjirsm.ac.cn
[c] Fujian Science & Technology Innovation Laboratory for Optoelectronic Information of China, Fuzhou, Fujian, 350108, China
[d] School of Applied Physics and Materials, Wuyi University, Jiangmen, Guangdong, 529020, China

† Electronic supplementary information (ESI) available. See DOI: https://doi.org/10.1039/d4tc03017f

‡ Ping Sui and Wei Zhang contributed equally.

medical diagnostics, the better tissue penetration depth will enhance the signal-to-noise ratio, making the diagnosis more reliable.[28,29] With this in mind, the development of a high-power broadband phosphor-converted NIR LD appears to be an advisable choice.[30–33] Being free of the ''efficiency droop'' enables the attainability of high output power by directly increasing the input current; meanwhile the broadband feature derived from the NIR phosphor expands the use of NIR spectroscopy applications. Such a scheme is particularly suitable for non-destructive analysis and identification of organics or biological imaging, where the abundant absorption bands of organic substances could be matched.

One of the major challenges of broadband phosphor-converted NIR LDs is the shortage of suitable NIR phosphor color converters, similar to the case of NIR LEDs, in view of the stringent performance metrics of high quantum efficiency (QE), low thermal quenching, wide bandwidth, the high resistance to blue laser irradiation and high luminescence saturation threshold. Researchers have screened NIR-emitting phosphors for NIR LEDs, among which chromium ion (Cr^{3+})-activated garnet-type structure phosphors were considered as ideal candidates;[34–37] however, these garnet phosphors cannot be directly used as color converters for NIR LDs. In order to cope with the harsh working conditions induced by high-power-density laser irradiation, it is imperative to fabricate NIR phosphor powder into an all-inorganic bulk form, among which the ''phosphor-in-glass'' (PiG) composite is praised for its design flexibility, low cost, and easy fabrication and has attracted great attention recently.[38–42] The fabrication of PiG in the form of a film to be deposited on a high-thermal-conductivity substrate will benefit the dissipation of huge heat upon laser irradiation.[43–46]

In this work, we developed a new kind of $Ca_3Sc_2Si_3O_{12}$:Ce^{3+},Cr^{3+},Li^+ (CSSO:Ce,Cr,Li) PiG film sintered on a sapphire plate (hereafter, abbreviated as CSSO:Ce,Cr,Li PiGF-on-SP). CSSO possesses a thermally and chemically stable garnet-type structure and shows good ability to accommodate a variety of luminescent centers including rare earth ions and transition metal ions. CSSO:Cr^{3+} has been demonstrated as a good candidate for NIR LEDs, and CSSO:Ce^{3+} is usually regarded as an efficient color converter to compensate for the ''cyan cavity'' in solid-state white lighting.[47–50] We did not deliberately look for a new phosphor, but tried to optimize the existing one to make it qualify for high-power-density NIR LD illumination. The selection of CSSO:Ce,Cr,Li is based on the overall consideration of the achievable high QE and good thermal stability. The introduction of Ce helps to increase the absorption efficiency of the blue laser, and the addition of Li compensates for the charge imbalance and also acts as a flux to improve crystallinity. A systematic study of the material fabrication and the microstructural and spectroscopic properties of the CSSO:Ce,Cr,Li PiGF-on-SP composites was carried out. The luminescence saturation effect under blue laser irradiation was carefully examined. Some potential applications for food safety assurance, night vision enhancement, and tissue detection were tentatively demonstrated.

2. Experimental

2.1. Synthesis of CSSO:Ce,Cr,Li phosphors

CSSO:Ce,Cr,Li phosphors were synthesized by a high-temperature solid-phase method. $CaCO_3$ (AR), Sc_2O_3 (AR), SiO_2 (AR), Cr_2O_3 (AR) and CeO_2 (AR) were weighed according to the stoichiometric ratio and were wet-ground in an agate mortar with different amounts of flux Li_2CO_3 (AR) and an appropriate amount of anhydrous ethanol for 20 min to evenly mix them. The mixture was then transferred to a clean alumina crucible, placed in a tube furnace, held at 1450 °C for 3 h in a mixture of 95% N_2/5% H_2, and cooled to room temperature in the furnace. Finally, CSSO:Ce,Cr,Li powder samples were obtained and were used as phosphors for the subsequent preparation of PiGF.

2.2. Preparation of PiGF

The low melting point glass powder, organic vehicles and CSSO:Ce,Cr,Li phosphor were mixed at a certain mass ratio, and the slurry was evenly scraped and coated on a 1 × 1 cm transparent sapphire substrate with a coater. The organic binder was discharged from PiGF in an oven at 130 °C for 24 h and then heat treated in a muffle furnace at different temperatures and times (620 °C and 0–50 min). By adjusting the PiGF thickness and the ratio of the CSSO:Ce,Cr,Li phosphor to glass powder, CSSO:Ce,Cr,Li PiGF composites with excellent properties were obtained.

2.3. Characterization

X-ray diffraction (XRD) patterns were collected by using an X-ray diffractometer (Miniflex600, Cu Kα, Rigaku). The glass transition temperature was measured using a differential scanning calorimeter (DSC, Netzsch, STA449F3) at a heating rate of 10 °C min^{-1} in an air atmosphere. The microscopic morphology was observed by using a scanning electron microscope (SEM, JEOL, JSM-7600F). The elemental distribution in the PiG film was detected by energy-dispersive spectroscopy (EDS) and X-ray fluorescence (XRF) spectroscopy (Bruker, M4 Tornado). Photoluminescence (PL), PL excitation (PLE), and fluorescence decay curves were measured using a fluorescence spectrometer (Edinburgh Instruments, FLS920) equipped with a xenon lamp and a 475 nm pulsed laser light source. For the temperature-dependent PL, the sample was placed on a cooling–heating stage (77–873 K, THMS600E, Linkam Scientific Instruments) with the excitation/emission light transmitted *via* optical fibers. The luminescence quantum efficiency (QE) was measured using an FLS920, optical fiber spectrometer, and an integrating sphere. The photometric and colorimetric parameters of samples under blue LD excitation were collected using a self-built laser illumination system, consisting of a customized integrating sphere, a 22 W blue laser (Ningbo Yuanming Optoelectronics, LSR455CP) and a fiber spectrometer (Ocean Optics, QEpro). The optical power of the blue laser was measured by using a laser power meter with a thermopile power probe (30A-BB-18, Ophir). The surface temperature of the sample was

measured using an infrared thermal imaging camera (TIS75, Fluke).

3. Results and discussion

CSSO:Ce,Cr,Li phosphor powders were synthesized *via* a solid-state sintering method under a reductive atmosphere (see the Experimental section). X-ray diffraction (XRD) patterns demonstrate the main phase of CSSO (PDF No. 72-1969) and a small amount of impurity phases of Sc_2O_3 and SiO_2 regardless of the variation in Ce or Cr doping content (Fig. S1a, ESI†). Similar to previous reports,[51,52] these impurities were very difficult to remove, but they exerted little influence on the luminescence properties. The introduction of Li^+ reduces the impurity content and increases the crystallinity (Fig. S1b, ESI†), thanks to its role as a flux to improve mass transfer during sintering.[53] Cr^{3+} (r = 0.615 Å, CN = 6) occupies the Sc^{3+} (r = 0.745 Å, CN = 6) site in the [ScO_6] octahedron,[51,52] while Ce^{3+} (r = 1.143 Å, CN = 8) occupies the Ca^{2+} (r = 1.12 Å, CN = 8) site in the [CaO_8] dodecahedron.[54] The observed gradual XRD peak shifts towards high- and low-angle directions with increasing Cr^{3+} and Ce^{3+} contents, respectively, supporting the above occupancy site attributions. The substitution of Ca^{2+} with Ce^{3+} causes a charge imbalance which can be compensated by Li^+ *via* $2Ca^{2+} \rightarrow Ce^{3+} + Li^+$.[55,56] The doping contents of Ce^{3+}, Cr^{3+} and Li^+ were optimized to 7 mol%, 4 mol% and 0.5 wt%, respectively, attaining the highest NIR emission intensity of Cr^{3+} (Fig. S2, ESI†).

The optimized CSSO:Ce,Cr,Li phosphor powders were then co-sintered with SiO_2–Al_2O_3–ZnO–CaO–K_2O silicate glass powders on a sapphire plate to form a CSSO:Ce,Cr,Li PiGF-on-SP composite (Experimental section). To produce high-quality luminescent PiGF, the glass powders should soften and wet the phosphor powders, thus good flowability is required by elevating the sintering temperature. However, the sample should not be overheated, otherwise, serious thermal corrosion at the interfaces between the phosphor and glass will deteriorate the luminescence performance. Given these circumstances, the co-sintering procedure parameters, including the sintering temperature (T_s) and holding time (t_s), were first optimized. The appearances of the bare glass films sintered on SP with varying T_s or t_s are presented in Fig. 1a and b. When T_s is lower than 600 °C, the glass is too viscous to flow, so the glass film rich in open pores looks almost opaque. As T_s is increased above 600 °C, the transparency of the glass film is greatly improved due to the increase of the densification degree; however, as T_s is further increased higher than 620 °C, the trend reverses, probably because of the newly generated pores due to the occurrence of oxide volatilization. The maximum transparency reaches 75% at 450 nm (Fig. 1c and d). On the other hand, when T_s is fixed at 620 °C and t_s is varied from 0 min to 50 min, there is no obvious difference in the appearance of the bare glass film on SP, as well as in the measured transparency (Fig. 1e and f). The difference occurs when fabricating CSSO:Ce,Cr,Li PiGF-on-SP with varying t_s, where the English words behind the PiGF-on-SP plate appear clearest for the t_s = 40 min sample (the inset of Fig. 1g). Unlike

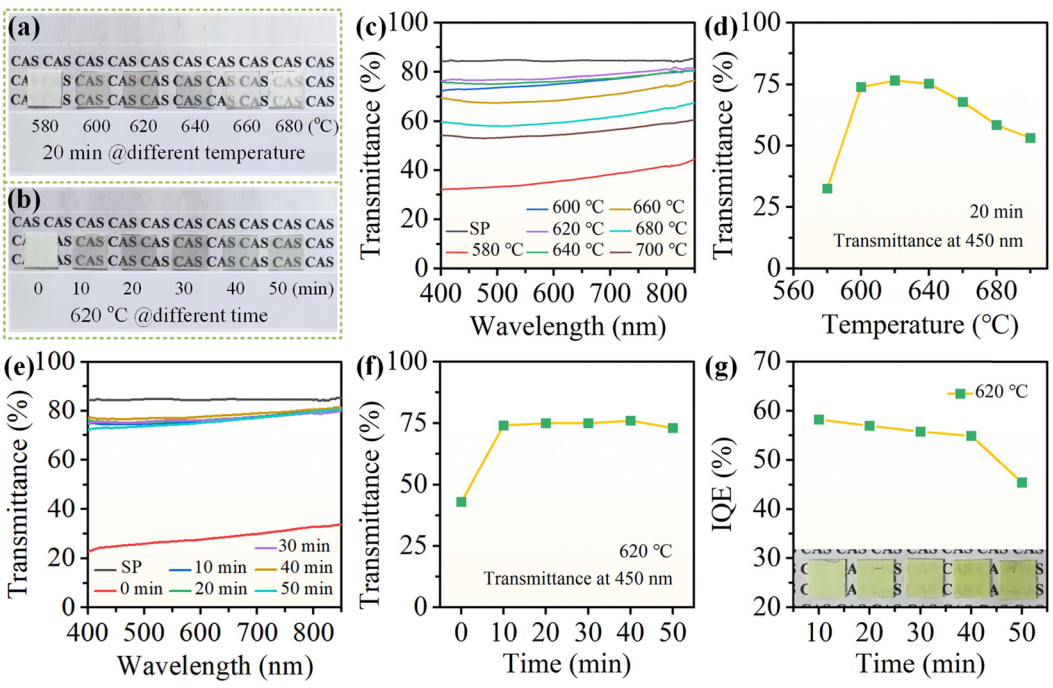

Fig. 1 Photographs of the bare glass film sintered on SP with (a) varying sintering temperatures at 20 min and (b) sintering times at 620 °C. Total transmittance spectra of (c) the SP substrate and the bare glass film on SP treated at different temperatures for 20 min and (e) the bare glass film on SP treated at 620 °C for different holding times. (d) and (f) The transmittance variation at 450 nm in (c) and (e). (g) The sintering time-dependent IQE variation in the CSSO:Ce, Cr, Li PiGF-on-SP composite; the insets show the photographs of samples.

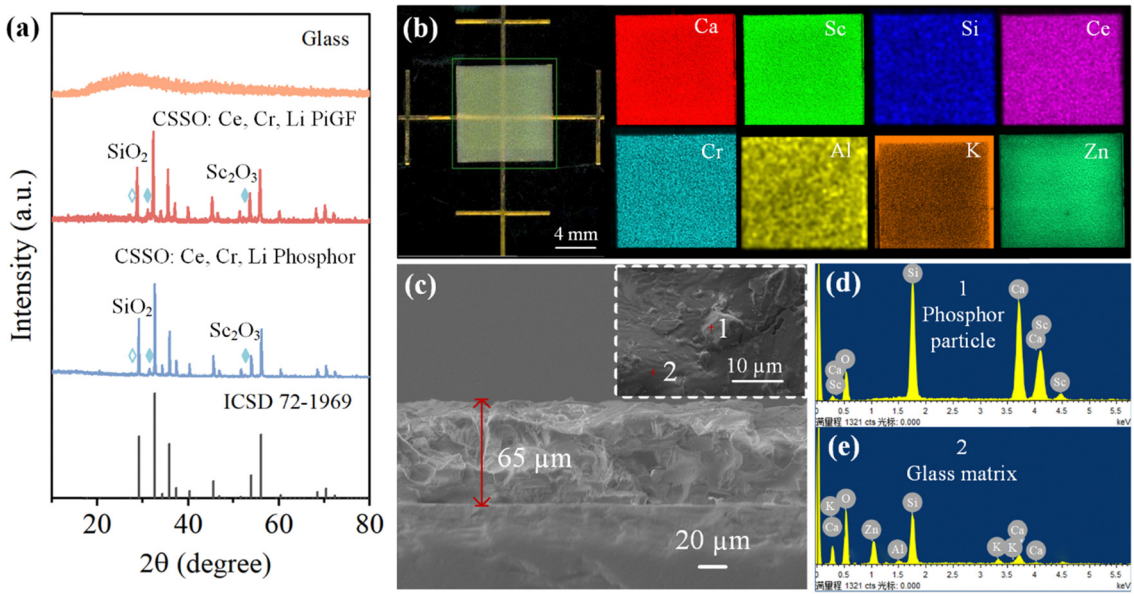

Fig. 2 (a) XRD patterns of glass powders, CSSO:Ce,Cr,Li phosphor powders and corresponding CSSO:Ce,Cr,Li PiGF on SP. (b) XRF measurement showing macroscopically the homogeneous chemical distributions of chemical elements in PiGF. (c) SEM image of the cross section of the PiGF-on-SP composite; the inset shows the embedded phosphor particles. EDS spot analyses on two spots labelled in the inset of (c).

the easily cohesive glass powders, the heterogeneous wetting of phosphor powders by viscous glass and the expulsion of pores between them consumes time. The t_s-dependent internal QE (IQE) shows a slight decline before 50 min and a rapid decrease thereafter. The combination of phosphor particles and the glass matrix is usually accompanied by ionic diffusion leading to thermal corrosion.[57] The co-sintering procedure of the CSSO:Ce,Cr,Li PiGF-on-SP composite is finally optimized to 620 °C for 40 min, which was adopted in the subsequent experiments.

In Fig. 2a, the XRD pattern of the glass powders shows a typical amorphous hump structure. After compounding with CSSO:Ce,Cr,Li, the PiGF composite exhibits identical crystalline diffraction peaks to those of the original phosphor powders, including the CSSO:Ce,Cr,Li main phase (ICSD 72-1969) and the Sc_2O_3 plus SiO_2 impurity phases. No additional impurity phase is produced after co-sintering. X-ray fluorescence (XRF) spectra in Fig. 2b macroscopically exhibit the homogeneous chemical distributions of Ca, Sc, Si, Ce, Cr, Al, K, and Zn elements, demonstrating that CSSO:Ce,Cr,Li phosphor particles are well dispersed in the glass matrix without any obvious particle agglomeration. Microscopic observation by scanning electron microscopy (SEM) and complementary energy-dispersive X-ray spectroscopy (EDS) reveals dense wrapping of phosphor particles by a glass matrix with no perceivable pores. The binding of PiGF to the substrate is so strong that scratching with fingernails cannot easily peel off the thick film, which is also reflected by the tight contact between them by SEM observation of the cross section (Fig. 2c). CSSO:Ce,Cr,Li phosphor particles are randomly distributed in the glass matrix. EDS spot analysis distinguishes the phosphor particles from the glass matrix in terms of their different chemical compositions (Fig. 2d and e).

Spectroscopic studies showed that both of CSSO:Ce,Li and CSSO:Cr yield broad excitation bands in the blue region matching the commercial blue LD chip (Fig. S3a, ESI†). Under 450 nm excitation, one can observe the typical Ce^{3+}: $5d_1 \rightarrow 4f$ ($^2F_{5/2}$, $^2F_{7/2}$) cyan emission from CSSO:Ce and the Cr^{3+}: $^4T_{2g} \rightarrow {}^4A_{2g}$ (^4F) NIR emission from CSSO:Cr. In the CSSO garnet, Ce^{3+} occupies the dodecahedral site of Ca^{2+}, which has almost the same strong crystal field strength as that in YAG;[58,59] while Cr^{3+} impurity ions occupy intermediate field sites of Sc^{3+} in the lattice with $D_q/B = 2.25$.[60,61] There is an efficient energy transfer (ET) from Ce^{3+} to Cr^{3+}, alleviating the weak absorption problem of Cr^{3+} in the blue region due to the parity-forbidden nature of Cr^{3+}: 5d ↔ 5d transitions. The ET efficiency is calculated to be 68.3% based on the lifetime data (Fig. S3b, ESI†). In Fig. 3a, the CSSO:Ce,Cr,Li phosphor and the corresponding PiGF-on-SP composite show both the intense Ce^{3+}: 4f → 5d excitation band as well as the relatively weak Cr^{3+}: $^4A_2 \rightarrow {}^4T_1$ and $^4T_2$ excitation bands by monitoring the Cr^{3+} emission at 780 nm; the NIR emission is much stronger under blue light excitation compared to the visible emission. It is to be noted that the spectroscopic properties, including the spectral profile, luminescence decay (~0.12 ms), IQE (slight variation: 58% → 55%), and EQE (slight variation: 37% → 35%), from the phosphor are well preserved in the PiGF composite (Fig. 3a–c), which further confirms the insignificant thermal corrosion between the phosphor and glass components during co-sintering. In particular, the observation of identical photoluminescence decay curves of the CSSO:Ce,Cr,Li phosphor by monitoring the Cr^{3+} emission at different wavelengths (Fig. S4, ESI†) confirms the single luminescent center of Cr^{3+} in the CSSO:Ce,Cr,Li phosphor and eliminates the interference of impurities in the phosphor on the luminescence characteristics of the phosphors. The thermal stability examination shows an even better

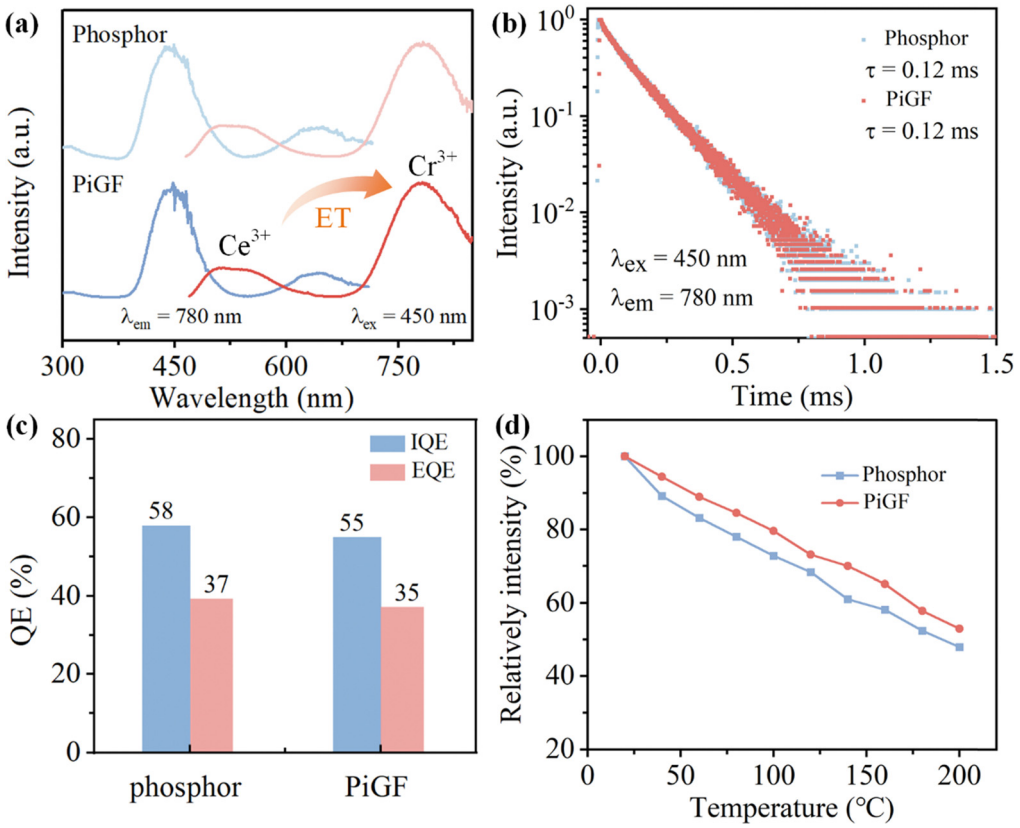

Fig. 3 (a) PL/PLE spectra (λ_{ex} = 450 nm; λ_{em} = 780 nm); (b) luminescence decay curves; and (c) QE and (d) temperature dependence of the integrated luminescence intensities of the CSSO:Ce,Cr,Li phosphor powders and the corresponding CSSO:Ce,Cr,Li PiGF-on-SP composite.

resistance to thermal quenching in the PiGF composite, where 70% of the luminescence intensity is retained at 150 °C relative to that at room temperature, which is basically in line with the requirements for laser-driven lighting.

The laser-driven luminescence properties of CSSO:Ce,Cr,Li PiGF were carefully evaluated using a self-built laser system capable of operating in either a static or rotatory excitation mode. By measuring through a transmissive optical path (Fig. 4a), the influences of sample parameters, *i.e.*, the thickness and weight ratio of phosphor to glass (P : G ratio), on the luminous performance were carefully examined. The spot size of the used blue laser is limited to $\approx$1 mm^2 through a series of focusing lenses. The dependences of the NIR output power (P_{out}) on the blue laser input power (P_{in}) of samples with a fixed P : G = 2 : 1 and various film thicknesses are presented in Fig. 4b. The variation trend differs in different P_{in} ranges: the 100 μm sample yields the brightest luminescence when P_{in} < 14 W mm^{-2}, while the 80 μm sample becomes the optimized one when P_{in} > 14 W mm^{-2}. The thickened film increases the number of excitable phosphor particles; but the thicker the film, the greater the Mie scattering, and, most importantly, the heavier the heat accumulation. It can be seen that the luminescence threshold drops rapidly from 18 W mm^{-2} to 6 W mm^{-2} due to thermal saturation.[40] The film thickness seems to be a decisive factor for the luminous performance as it determines the heat conduction path length to the sapphire plate from which the heat is dissipated into air. In Fig. 4c, the plot of NIR P_{out} *versus* P_{in}, with the film thickness fixed at 80 μm and increasing phosphor load, shows a similar decline in the luminescence threshold. There is no obvious luminescence saturation when P_{in} reaches 20 W mm^{-2} for the P : G = 1 : 2 sample, and it gradually decreases to ~12 W mm^{-2} for the P : G = 10 : 1 sample. The higher phosphor load indicates more luminescent centers on one hand, but also more microheating sources (due to the Stokes shift during color conversion in micrometer-sized phosphor particles) on the other hand. That is why an optimal P : G ratio exists. The P_{in}-dependent EL spectra corresponding to the optimized sample with P : G = 6 : 1 and 80 μm thickness are depicted in Fig. 4d. The maximum attainable NIR P_{out} is 730 mW when saturated at 18 W mm^{-2} in this static transmissive excitation mode. The real-time recorded temperature variation in the laser spot shows the steady elevation from 29.6 °C to 225.7 °C. At 18 W mm^{-2}, the heat generated cannot be efficiently dissipated away, so the growth rate of NIR output cannot keep up with the decreasing rate due to thermal quenching, resulting in luminescence saturation at 225.7 °C.

The excitation of phosphor color converters in a reflective optical path is most frequently used in laser-driven lighting, whose configuration is advantageous for efficient thermal management by mounting the composite material on a heat sink (*e.g.*, an Al plate) with high thermal capacity.[62–64]

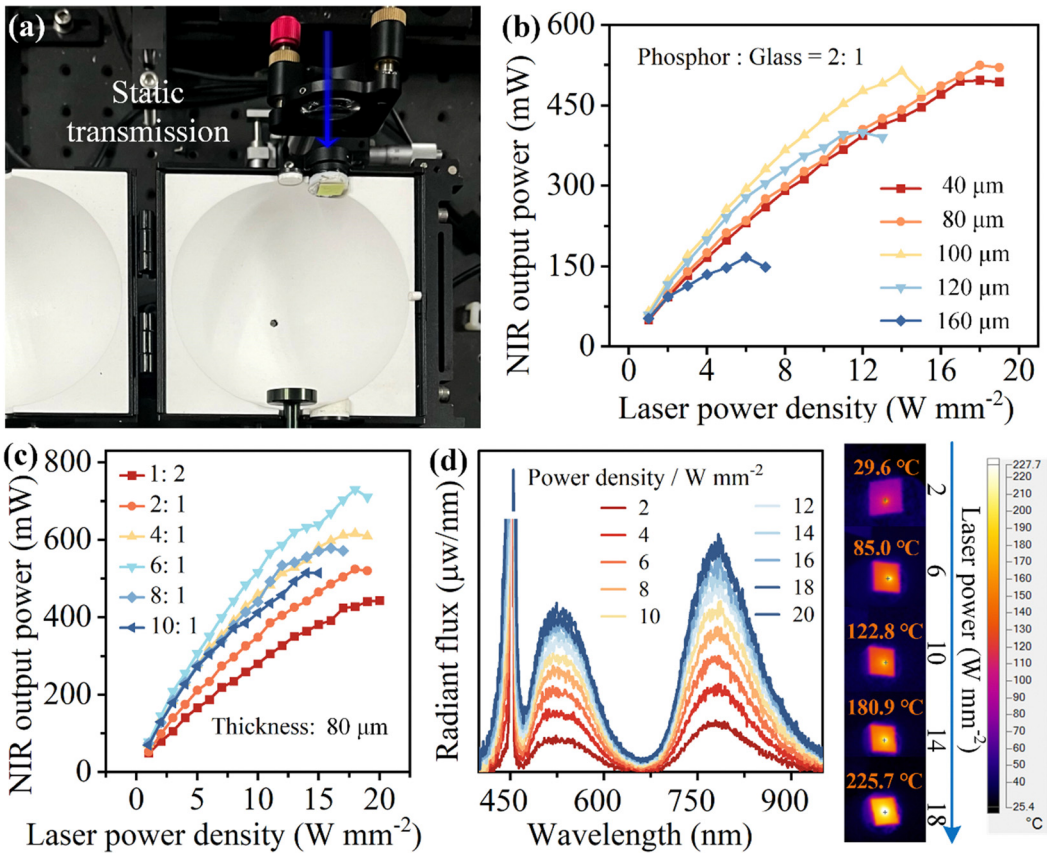

Fig. 4 (a) Digital photograph of the self-built laser system using a static transmission light path. The converted NIR light power *versus* incident laser power density in samples (b) with various thicknesses and (c) with various phosphor contents. (d) EL spectra of the optimal sample upon blue laser irradiation at different optical power densities and the temperature variation at the laser spot with increasing optical power densities from 2 to 18 W mm^{-2}.

By measuring through a reflective optical path (Fig. 5a), we examined the luminescence performance under static and rotating excitation. As shown in Fig. 5b, the luminescence saturation occurs at 20 W mm^{-2} with a maximum NIR P_{out} of up to 1021 mW for the static excitation mode, while no luminescence saturation is observed to the limit of the used blue LD with a NIR P_{out} of 1697 mW (22 W mm^{-2}), which is superior to those of most LED-driven NIR illumination ever reported (Table S1, ESI†). The "phosphor wheel" in the rotating excitation mode provides not only an additional heat dissipation path by boosting heat convection to the air, but also the pulsed excitation mode that greatly shortens the laser irradiation time, thus relieving both thermal quenching and intensity quenching. The P_{in}-dependent EL spectra in the rotating excitation mode demonstrate the continuous growth of the EL intensity (Fig. 5c) and a marginal temperature elevation at the laser spot (Fig. 5d) as P_{in} increases.

The "phosphor wheel" configuration also provides a good entry point to study the phenomenon of luminescence saturation in phosphor color converters, as it almost eliminates the influence of thermal quenching, leaving only intensity quenching.[65] In Fig. 6a and b, we compared the P_{in}-dependent relative conversion efficiencies (CE, η_{CE}) in static and rotating excitation modes in the reflective optical path. The CE can be calculated using the expression:[66]

$$\eta_{CE} = \frac{P_{em}}{P_{ab}} = \frac{P_{em}}{P_{in} - P_{re}} \quad (1)$$

where P_{in} is the incident blue laser optical power recorded using a laser power meter, and P_{re} is the remaining blue light optical power (P_{in} minus P_{ab}, which is the optical power absorbed by phosphor color converters) measured using an integrating sphere. The CEs for Ce^{3+} and Cr^{3+} are calculated and then plotted in these figures to distinguish their different luminescence behaviors. The CE of Ce^{3+} decreased rapidly in the static excitation mode, while the decline was greatly slowed down in the rotating excitation mode. The CE decreasing trends of Cr^{3+} in these two modes did not differ significantly, except for a sudden drop at the saturation point. Bearing in mind that the "phosphor wheel" almost excludes thermal quenching, one can conclude that the Ce^{3+} luminescence variation is more sensitive to heat and the Cr^{3+} luminescence variation is more sensitive to the incident blue photons. The contributions of thermal quenching and intensity quenching at different P_{in} values in the static excitation mode are calculated and plotted in Fig. 6c and d, from which it can be seen that the thermal

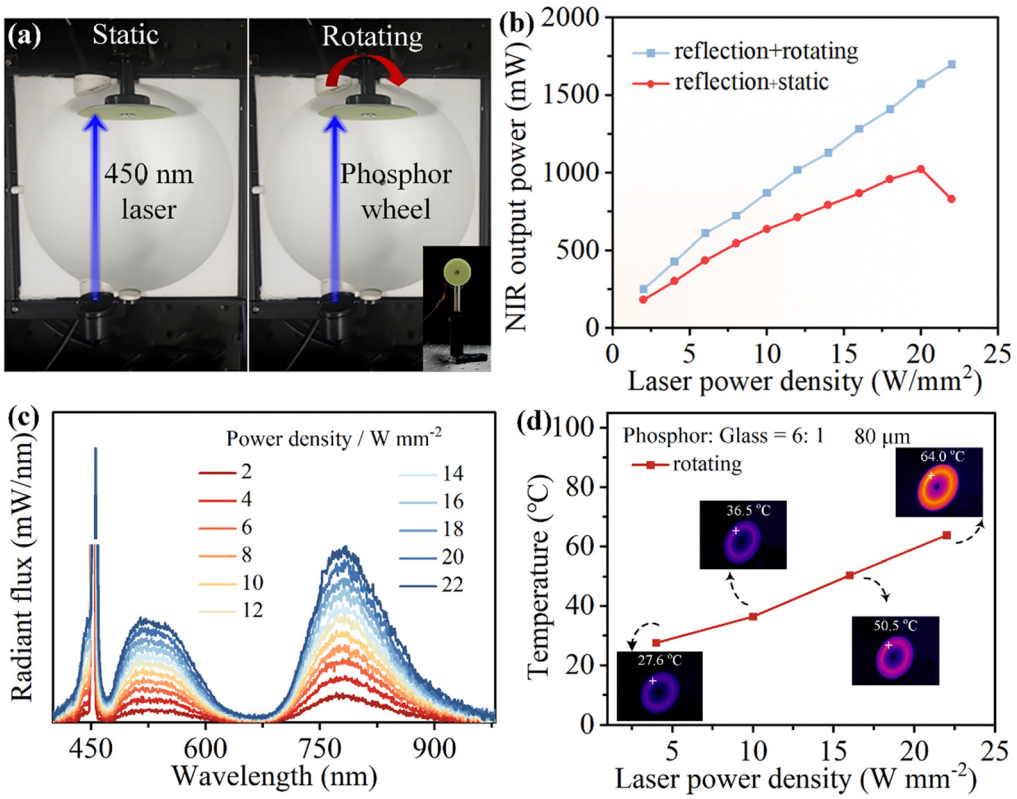

Fig. 5 (a) Digital photograph of the self-built laser system using a reflective light path and the fabricated phosphor wheel installed inside an integrating sphere. (b) P_{in}-dependent NIR output power of the optimal CSSO:Ce,Cr,Li PiGF-on-sapphire sample in static and rotating excitation modes. (c) EL spectra of the phosphor wheel when rotating under blue laser irradiation at different P_{in} values. (d) The P_{in}-dependent real-time temperature at the laser spot when rotating.

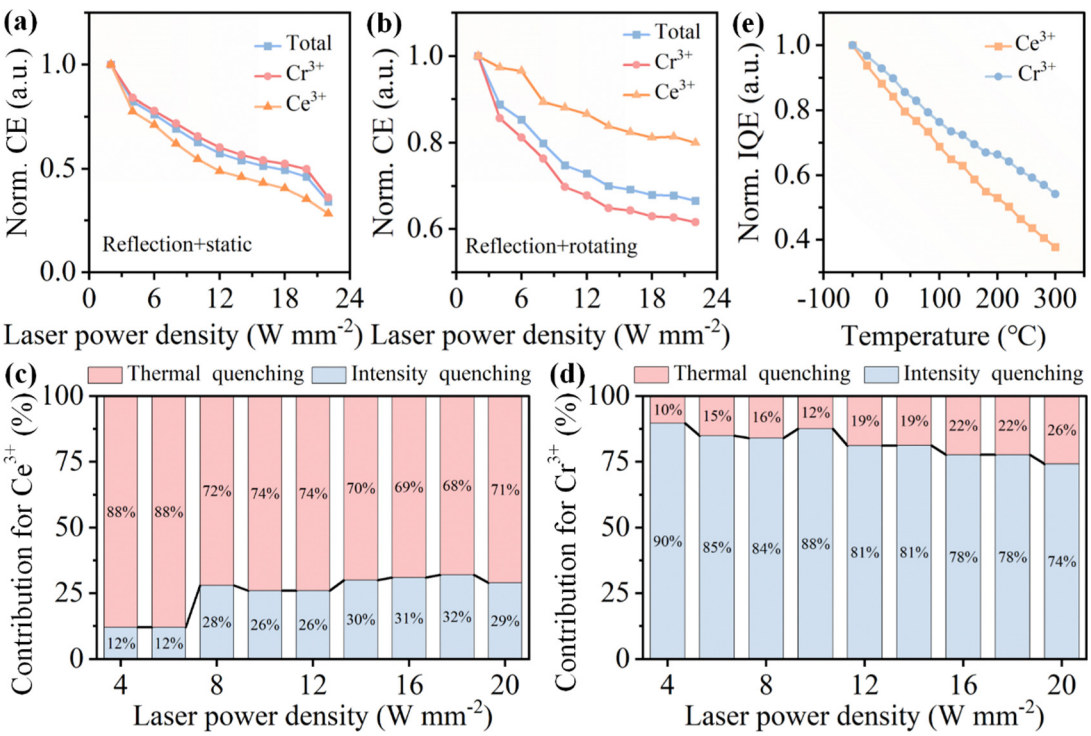

Fig. 6 P_{in}-dependent relative conversion efficiencies of Ce^{3+} and Cr^{3+} in the PiGF sample in a reflective optical path in (a) static and (b) rotating excitation modes. The calculated contributions from thermal quenching and optical quenching for (c) Ce^{3+} and (d) Cr^{3+}. (e) The temperature-dependent relative IQEs for Ce^{3+} and Cr^{3+}.

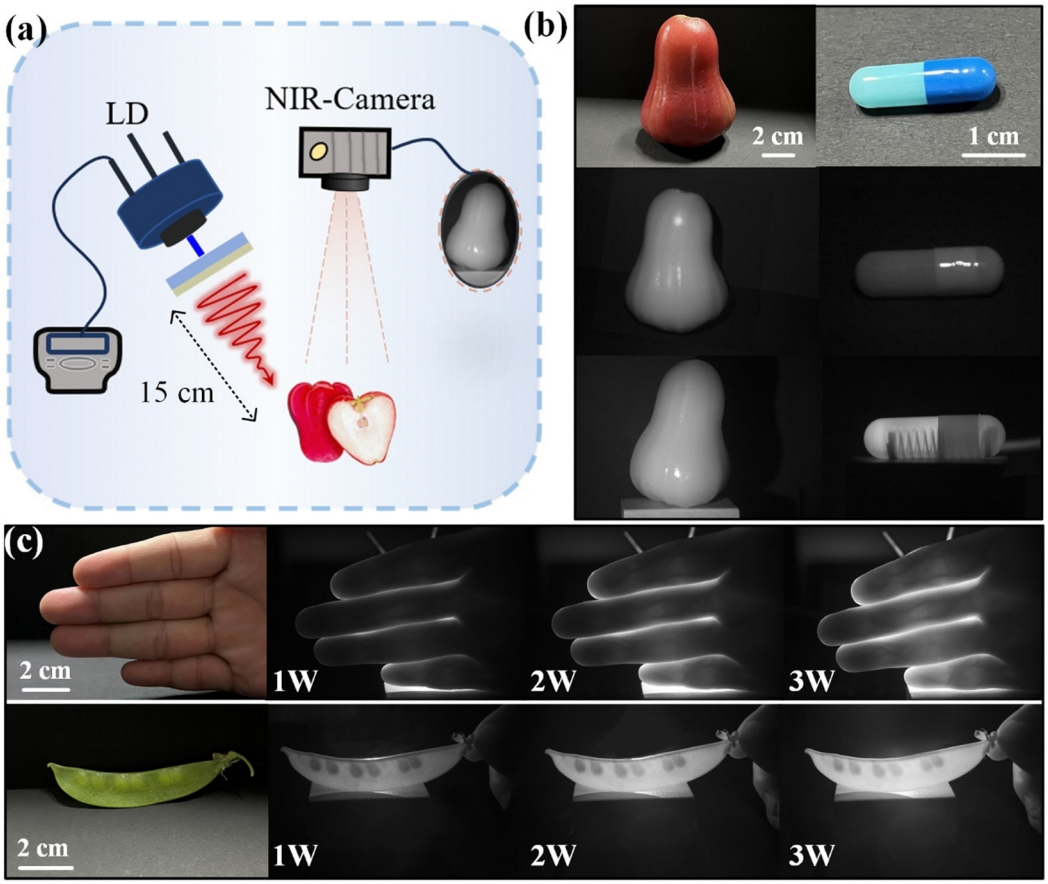

Fig. 7 (a) Schematic illustration of the imaging system based on the fabricated NIR light source, (b) comparison of the imaging effect of Jambu air and a spring-loaded capsule under a fluorescent lamp, commercial NIR-LED and the fabricated PiGF-based LD light source respectively (the illumination distances were all fixed at 15 cm). (c) Imaging effects of the hand and bean at different LD powers.

quenching and the intensity quenching account for 71% and 29% for Ce^{3+} and 26% and 74% for Cr^{3+} when the luminescence saturation occurs at 20 W mm^{-2}. Cr^{3+} possesses a much longer microsecond lifetime, which should be responsible for the ease of suffering from intensity quenching since the electrons in the excited state have a great chance of being promoted to the conduction band and eventually quenched by defect centers. The temperature-dependent relative IQE values for Ce^{3+} and Cr^{3+} are also measured and plotted in Fig. 6e. The IQE measurement is performed under low blue light photon flux, so that intensity quenching can be excluded. IQE is proportional to CE, but CE takes the Stokes shift loss into account. The decrease in IQE with increasing temperature is almost linear, so the temperature-dependent CE should be the same if only thermal quenching occurs during high-power laser irradiation. In fact, the decrease in CE appears to be exponential, which is influenced by intensity quenching. The interaction of excited-state ions, *e.g.*, ET upconversion, during the high-power-density laser excitation process should result in the exponential decay behavior.[67]

Finally, to validate the imaging effectiveness of NIR LDs, we constructed an NIR LD imaging setup (as schematically depicted in Fig. 7a). The target object is positioned beneath a PiGF-based light source powered by a blue laser and captured using a NIR camera. Fig. 7b shows the imaging outcomes of Jambu air and a spring-loaded capsule under a fluorescent lamp, a commercial NIR LED with an optical output of ~420 mW, and a NIR LD with identical input power density (1 W), respectively. It is observed that the imaging quality under the LD light source is much better, and importantly, the spring inside the capsule is clearly displayed, thereby substantiating the enhanced penetration effect of the LD. Furthermore, by varying the input power of the NIR LD from 1–3 W, distinct imaging effects were observed for both hand and Dutch beans at different power levels. The results demonstrate an improved imaging contrast as the power increases (Fig. 7c). Obviously, the CSSO PiGF LD may find potential applications in the fields of food safety assurance, night vision enhancement, tissue detection, *etc.*

4. Conclusions

In summary, CSSO:Ce,Cr,Li PiGF-on-SP composites were designed and fabricated for advanced laser-driven NIR lighting. Elaborate experiments were performed to optimize the sintering

parameters, film thickness, and phosphor loading. Microstructural and luminescence analyses demonstrate that glass components react trivially with phosphor particles during co-sintering, which ensures the preservation of the spectroscopic properties of phosphor particles. The CSSO:Ce,Cr,Li PiGF-on-SP composite yields a good IQE of 55% and retains 70% of the luminescence intensity at 150 °C. In the static excitation mode, the luminescence saturates at 18 W mm^{-2} (transmissive mode) and 20 W mm^{-2} (reflective mode), attaining maximal NIR outputs of 730 mW and 1021 mW, respectively, when driven by a blue laser, which is much superior to that of the NIR pc-LED counterparts. In the rotating excitation mode, no luminescence saturation is observed up to the limit of the used blue LD used with a NIR output of 1697 mW (22 W mm^{-2}). Probing into the luminescence saturation mechanism shows that thermal quenching and intensity quenching account for 71% and 29% of Ce^{3+} and 26% and 74% of Cr^{3+}, when luminescence saturation occurs. The proof-of-concept experiments demonstrate that the developed NIR-emissive PiGF composite satisfies various NIR lighting application scenarios.

Data availability

Data for this article, including the original microstructural and spectroscopic data, are available on request from the corresponding authors Hang Lin (lingh@fjirsm.ac.cn) or Yuansheng Wang (yswang@fjirsm.ac.cn).

Conflicts of interest

There are no conflicts to declare.

Acknowledgements

This work was supported by the National Natural Science Foundation of China (52372161, U2005213 and 12274408), the Science Fund for Distinguished Young Scholars of Fujian Province (2022J06030), the Science Fund of Fujian Province (2023J01217), the Fujian Science & Technology Innovation Laboratory for Optoelectronic Information of China (2021ZR134), and the STS Project of Fujian-CAS (2022T3069).

References

1 Y. Y. Gu, Z. Y. Guo, W. Yuan, M. Y. Kong, Y. L. Liu, Y. T. Liu, Y. L. Gao, W. Feng, F. Wang, J. J. Zhou, D. Y. Jin and F. Y. Li, High-Sensitivity Imaging of Time-Domain Near-Infrared Light Transducer, *Nat. Photonics*, 2019, **13**, 525–531.
2 C. Pasquini, Near Infrared spectroscopy: A Mature Analytical Technique with New Perspectives – A Review, *Anal. Chim. Acta*, 2018, **1026**, 8–36.
3 V. Rajendran, M. H. Fang, G. N. D. Guzman, T. Lesniewski, S. Mahlik, M. Grinberg, G. Leniec, S. M. Kaczmarek, Y. S. Lin, K. M. Lu, C. M. Lin, H. Chang, S. F. Hu and R. S. Liu, Super Broadband Near-Infrared Phosphors with High Radiant Flux as Future Light Sources for Spectroscopy Applications, *ACS Energy Lett.*, 2018, **3**, 2679–2684.
4 M. Vasilopoulou, A. Fakharuddin, F. P. García de Arquer, D. G. Georgiadou, H. Kim, A. R. B. Mohd Yusoff, F. Gao, M. K. Nazeeruddin, H. J. Bolink and E. H. Sargent, Advances in Solution-Processed Near-Infrared Light-Emitting Diodes, *Nat. Photonics*, 2021, **15**, 656–669.
5 G. C. Liu and Z. G. Xia, Modulation of Thermally Stable Photoluminescence in Cr^{3+}-Based Near-Infrared Phosphors, *J. Phys. Chem. Lett.*, 2022, **13**, 5001–5008.
6 Y. Lv, Y. K. Li, Z. Y. Li and R. J. Xie, Near-Infrared Emission of Sm^{2+} in Oxynitrides, *Adv. Opt. Mater.*, 2023, **12**, 2302303.
7 D. C. Huang, H. M. Zhu, Z. H. Deng, H. Y. Yang, J. Hu, S. S. Liang, D. J. Chen, E. Ma and W. Guo, A Highly Efficient and Thermally Stable Broadband Cr^{3+}-Activated Double Borate Phosphor for Near-Infrared Light-Emitting Diodes, *J. Mater. Chem. C*, 2021, **9**, 164–172.
8 L. L. Zhang, S. Zhang, Z. D. Hao, X. Zhang, G. H. Pan, Y. S. Luo, H. J. Wu and J. H. Zhang, A High Efficiency Broad-Band Near-Infrared $Ca_2LuZr_2Al_3O_{12}$: Cr^{3+} Garnet Phosphor for Blue LED Chips, *J. Mater. Chem. C*, 2018, **6**, 4967–4976.
9 J. W. Qiao, G. J. Zhou, Y. Zhou, Q. Y. Zhang and Z. G. Xia, Divalent Europium-Doped Near-Infrared-Emitting Phosphor for Light-Emitting Diodes, *Nat. Commun.*, 2019, **10**, 5267.
10 F. Y. Zhao, Y. H. Shao, Q. L. Liu and J. S. Zhong, Blue-Light-Excitable Broadband $Ca_3Ga_2Ge_3O_{12}$: Cr^{3+}, Ni^{2+} Phosphor for the Applications in NIR-II Window, *Laser Photonics Rev.*, 2024, **18**, 2400447.
11 X. F. Zhou, W. Y. Geng, J. Y. Li, Y. C. Wang, J. Y. Ding and Y. H. Wang, An Ultraviolet–Visible and Near-Infrared-Responded Broadband NIR Phosphor and Its NIR Spectroscopy Application, *Adv. Opt. Mater.*, 2020, **8**, 1902003.
12 K. P. Guo, M. Righetto, A. Minotto, A. Zampetti and F. Cacialli, Non-Toxic Near-Infrared Light-Emitting Diodes, *iScience*, 2021, **24**, 102545.
13 Z. Y. Yang, T. de Boer, P. M. Braun, B. B. Su, Q. Y. Zhang, A. Moewes and Z. G. Xia, Thermally Stable Red-Emitting Oxide Ceramics for Laser Lighting, *Adv. Mater.*, 2023, **35**, 2301837.
14 W. B. Chen, Y. Z. Wang, J. Xu, X. R. Chen, O. B. Jensen, Q. Y. Zhang and Z. G. Xia, Red-Emitting Cordierite Ceramic Enabling General Healthy Warm White Laser Lighting, *Laser Photonics Rev.*, 2023, **18**, 2300963.
15 Y. S. Sun, Y. Z. Wang, W. B. Chen, Q. Q. Jiang, D. D. Chen, G. P. Dong and Z. G. Xia, Rapid Synthesis of Phosphor-Glass Composites in Seconds Based on Particle Self-Stabilization, *Nat. Commun.*, 2024, **15**, 1033.
16 J. Cho, E. F. Schubert and J. K. Kim, Efficiency Droop in Light-Emitting Diodes: Challenges and Countermeasures, *Laser Photonics Rev.*, 2013, **7**, 408–421.
17 S. P. DenBaars, D. Feezell, K. Kelchner, S. Pimputkar, C. C. Pan, C. C. Yen, S. Tanaka, Y. J. Zhao, N. Pfaff, R. Farrell, M. Iza, S. Keller, U. Mishra, J. S. Speck and S. Nakamura, Development of gallium-nitride-based light-emitting diodes (LEDs) and laser diodes for energy-efficient lighting and displays, *Acta Mater.*, 2013, **61**, 945–951.

18 J. Y. Tsao, M. H. Crawford, M. E. Coltrin, A. J. Fischer, D. D. Koleske, G. S. Subramania, G. T. Wang, J. J. Wierer and R. F. Karlicek, Toward Smart and Ultra-efficient Solid-State Lighting, *Adv. Opt. Mater.*, 2014, **2**, 809–836.

19 J. J. Wierer, J. Y. Tsao and D. S. Sizov, Comparison Between Blue Lasers and Light-Emitting Diodes for Future Solid-State Lighting, *Laser Photonics Rev.*, 2013, **7**, 963–993.

20 E. Belloni, F. Cotana, S. Nakamura, A. L. Pisello and D. Villacci, A New Smart Laser Photoluminescent Light (LPL) Technology for The Optimization of The On-Street Lighting Performance and the Maximum Energy Saving: Development of A Prototype and Field Tests, *Sustainable Energy Grids*, 2023, **34**, 101064.

21 L. L. Zhang, D. D. Wang, Z. D. Hao, X. Zhang, G. H. Pan, H. J. Wu and J. H. Zhang, Cr^{3+}-Doped Broadband NIR Garnet Phosphor with Enhanced Luminescence and its Application in NIR Spectroscopy, *Adv. Opt. Mater.*, 2019, **7**, 1900185.

22 J. A. Lai, Z. X. Wang, Y. J. Wang, S. J. Cao, D. F. Wu, Y. Q. Zhou, K. An, J. Du, P. He and X. S. Tang, Highly Efficient Broadband Near-Infrared Emission in Cr^{3+}-Activated Organic Hafnium Chlorine for Multi-Optoelectronic Applications, *Adv. Opt. Mater.*, 2024, **12**, 2400437.

23 W. R. Wang, Z. Chen, G. L. Yu, Y. M. Zhang, C. Jiang and J. R. Qiu, Ultra-Broadband Near-Infrared Luminescence from a Vanadium-Activated Phosphate Glass, *Adv. Opt. Mater.*, 2024, **12**, 2300413.

24 G. J. Zheng, W. G. Xiao, H. J. Wu, J. H. Wu, X. F. Liu and J. R. Qiu, Near-Unity and Zero-Thermal-Quenching Far-Red-Emitting Composite Ceramics via Pressureless Glass Crystallization, *Laser Photonics Rev.*, 2021, **15**, 2100060.

25 H. Xiao, J. N. Zhang, L. L. Zhang, H. Wu, H. J. Wu, G. H. Pan, F. Liu and J. H. Zhang, Cr^{3+} Activated Garnet Phosphor with Efficient Blue to Far-Red Conversion for pc-LED, *Adv. Opt. Mater.*, 2021, **9**, 2101134.

26 J. W. Qiao, S. Zhang, X. Q. Zhou, W. B. Chen, R. Gautier and Z. G. Xia, Near-Infrared Light-Emitting Diodes Utilizing a Europium-Activated Calcium Oxide Phosphor with External Quantum Efficiency of Up to 54.7%, *Adv. Mater.*, 2022, **34**, 2201887.

27 Y. L. Ma, X. C. Li, L. Wu, C. Y. Shao, B. Q. Zhang, T. Pang, L. L. Lu, H. Qiu, Y. Tian, G. L. Wang, Y. B. Hui, Q. W. Guo and D. Q. Chen, Preparation of $(Lu,Y)_3(Al,Sc,Cr)_2Al_3O_{12}$ Phosphor Ceramics with High Thermal Stability for Near-Infrared LED/LD, *J. Adv. Ceram.*, 2024, **13**, 354–363.

28 H. J. Jiang, L. Y. Chen, G. J. Zheng, Z. H. Luo, X. H. Wu, Z. H. Liu, R. Y. Li, Y. F. Liu, P. Sun and J. Jiang, Ultra-Efficient GAGG: Cr^{3+} Ceramic Phosphor-Converted Laser Diode: A Promising High-Power Compact Near-Infrared Light Source Enabling Clear Imaging, *Adv. Opt. Mater.*, 2022, **10**, 2102741.

29 H. J. Zhang, Translucent Ceramic Enabling Next-Generation Lasing-Driven Near-Infrared Light Source, *Sci. China Mater.*, 2024, **67**, 1359–1360.

30 C. J. Zhang, L. Huang, J. Y. Wang, T. L. Zhou and R. J. Xie, Screening of Broadband Near-Infrared Cr^{3+}-Activated Phosphors Using Ce^{3+} as a Probe, *Chem. Mater.*, 2023, **35**, 2038–2046.

31 S. M. Gu, B. M. Liu, S. C. Si and J. Wang, Laser-Driven NIR Light Source Based on MgO: Cr^{3+}, Ni^{2+} Phosphor-in-Glass Film for NIR Spectroscopy Application, *J. Mater. Chem. C*, 2023, **11**, 9014–9022.

32 G. C. Liu, W. B. Chen, Z. Xiong, Y. Z. Wang, S. Zhang and Z. G. Xia, Laser-Driven Broadband Near-Infrared Light Source with Watt-Level Output, *Nat. Photonics*, 2024, **18**, 562–568.

33 X. Y. Zhang, P. F. Sang, C. Wei, S. H. Lin, J. Kang, Y. B. Li, B. H. Sun, Y. Li, F. A. Selim, C. M. Zhou, T. Y. Zhou, S. W. Chen, C. F. Shi, W. Strȩk, H. Chen and L. Zhang, Ce: $(Lu,Sr)_3(Al,Si)_5O_{12}$ Transparent Ceramics for High-Power White LEDs/LDs with Ultra-High Luminance Saturation Threshold, *J. Mater. Chem. C*, 2024, **12**, 6046–6055.

34 D. Y. Huang, Q. Y. Ouyang, H. Xiao, B. Wang, H. Z. Lian, Q. G. Zeng and J. Lin, Cr, Yb-Codoped $Ca_2LaHf_2Al_3O_{12}$ Garnet Phosphor: Electronic Structure, Broadband NIR Emission and Energy Transfer Properties, *Dalton Trans.*, 2021, **50**, 908–916.

35 Q. P. Du, J. Ueda and S. Tanabe, Influence of Trap Centers on Persistent Luminescence of Cr^{3+} or Yb^{3+} Co-Doped $Y_3Al_2Ga_3O_{12}$: Pr^{3+} Ceramic Phosphors, *J. Am. Ceram. Soc.*, 2024, **107**, 5524–5533.

36 Z. W. Li, G. Zhu, S. S. Li, W. Xu, Q. F. Bian, Y. Cong, M. He, X. X. Luo, S. Y. Xin and B. Dong, High-Performance NIR Emission in Chromium-Doped Garnet Phosphors Enabled by Structure and Excitation Regulation, *Laser Photonics Rev.*, 2023, **18**, 2300732.

37 D. J. Liu, G. G. Li, P. P. Dang, Q. Q. Zhang, Y. Wei, L. Qiu, H. Z. Lian, M. M. Shang and J. Lin, Valence Conversion and Site Reconstruction in Near-Infrared-Emitting Chromium-Activated Garnet for Simultaneous Enhancement of Quantum Efficiency and Thermal Stability, *Light: Sci. Appl.*, 2023, **12**, 248.

38 X. M. Yue, J. Xu, H. Lin, S. S. Lin, R. F. Li, B. Wang, Q. G. Huang, P. F. Wang, P. Sui, Y. Cheng and Y. S. Wang, β-SiAlON: Eu^{2+} Phosphor-in-Glass Film: An Efficient Laser-Driven Color Converter for High-Brightness Wide-Color-Gamut Projection Displays, *Laser Photonics Rev.*, 2021, **15**, 2100317.

39 K. Li, W. C. Zhang, L. Y. Niu, Y. Ye, J. Ren and C. Liu, Lead-Free Cesium Manganese Halide Nanocrystals Embedded Glasses for X-Ray Imaging, *Adv. Sci.*, 2022, **10**, 2204843.

40 S. X. Liao, S. L. Jin, T. Pang, S. S. Lin, Y. H. Zheng, R. H. Chen, G. Y. Xi, X. Y. Li, B. Zhuang, F. Huang and D. Q. Chen, Novel Color Converters for High Brightness Laser-Driven Projection Display: Transparent Ceramics–Glass Ceramics Film Composite, *Adv. Funct. Mater.*, 2023, **34**, 2307761.

41 S. X. Liao, Z. Z. Yang, J. D. Lin, S. X. Wang, J. W. Zhu, S. X. Chen, F. Huang, Y. H. Zheng and D. Q. Chen, A Hierarchical Structure Perovskite Quantum Dots Film for Laser-Driven Projection Display, *Adv. Funct. Mater.*, 2022, **33**, 2210558.

42 Q. G. Huang, H. Lin, B. Wang, S. S. Lin, P. F. Wang, P. Sui, J. Xu, Y. Cheng and Y. S. Wang, Patterned Glass Ceramic

Design for High-Brightness High-Color-Quality Laser-Driven Lightings, *J. Adv. Ceram.*, 2022, **11**, 862–873.

43 Z. K. Yu, J. Z. Zhao, J. X. Liu, Y. Mou, M. X. Chen and Y. Peng, Heat-Conducting LSN: Ce-In-Glass Film on Aln Substrate for High-Brightness Laser-Driven White Lighting, *Ceram. Int.*, 2022, **48**, 36531–36538.

44 Z. Z. Yang, S. Zheng, T. Pang, S. X. Liao, J. W. Zhu, J. D. Lin, F. Huang, Y. H. Zheng and D. Q. Chen, YAG: Ce PiGF@Alumina-Substrate in A Reflection Mode for High-Brightness Laser-Driven Projection Display, *Adv. Mater. Technol.*, 2023, **8**, 2300132.

45 Q. X. Wen, Y. Wang, C. Zhao, L. Xu, X. D. Wang, Y. S. Xu, S. Lin, X. J. Liang, J. P. Liu and W. D. Xiang, Ultrahigh Power Density LuAG:Ce Green Converters for High-Luminance Laser-Driven Solid State Lighting, *Laser Photonics Rev.*, 2023, **17**, 2200909.

46 S. S. Lin, H. Lin, P. F. Wang, P. Sui, H. Y. Yang, J. Xu, Y. Cheng and Y. S. Wang, An Orange-Yellow-Emitting $Lu_{2-x}Mg_2Al_{2-y}GaYSi_2O_{12}$: xCe^{3+} Phosphor-in-Glass Film for Laser-Driven White Light, *J. Mater. Chem. C*, 2023, **11**, 1530–1540.

47 S. K. Sharma, Y. C. Lin, I. Carrasco, T. Tingberg, M. Bettinelli and M. Karlsson, Weak Thermal Quenching of the Luminescence in the $Ca_3Sc_2Si_3O_{12}$: Ce^{3+} Garnet Phosphor, *J. Mater. Chem. C*, 2018, **6**, 8923–8933.

48 H. J. Wu, H. Wu, G. H. Pan, L. L. Zhang, Z. D. Hao and J. H. Zhang, Cyan-Green-Emitting $Ca_3Sc_2Si_3O_{12}$: Ce^{3+} Transparent Ceramics: A Promising Color Converter for High-Brightness Laser Lighting, *J. Adv. Ceram.*, 2023, **12**, 1731–1741.

49 H. J. Wu, G. H. Pan, Z. D. Hao, L. L. Zhang, H. Wu and J. H. Zhang, Highly Efficient and Thermally Robust Cyan-Green Phosphor-in-Glass Films for High-Brightness Laser Lighting, *J. Mater. Chem. C*, 2021, **9**, 12342–12352.

50 S. P. Feofilov, A. B. Kulinkin and N. M. Khaidukov, Zero-Phonon Line of $^4T_2$ -$^4A_2$ Luminescence Band Of Cr^{3+} Ions in $Ca_3Sc_2Si_3O_{12}$ Garnet Ceramics, *J. Lumin.*, 2020, **224**, 117284.

51 Z. W. Jia, C. X. Yuan, Y. F. Liu, X. J. Wang, P. Sun, L. Wang, H. C. Jiang and J. Jiang, Strategies to Approach High Performance in Cr^{3+}-Doped Phosphors for High-Power NIR-LED Light Sources, *Light: Sci. Appl.*, 2020, **9**, 86.

52 Z. W. Jia, C. X. Yuan, R. Y. Li, P. Sun, R. Dong, Y. F. Liu, L. Wang, H. C. Jiang and J. Jiang, Electron–Phonon Coupling Mechanisms of Broadband Near-Infrared Emissions From Cr^{3+} in the $Ca_3Sc_2Si_3O_{12}$ Garnet, *Phys. Chem. Chem. Phys.*, 2020, **22**, 10343–10350.

53 Y. S. Lei, Y. H. Li, C. C. F. Lu, Q. Z. Yan, Y. L. Wu, F. Babbe, H. X. Gong, S. Zhang, J. Y. Zhou, R. T. Wang, R. Q. Zhang, Y. M. Chen, H. Tsai, Y. Gu, H. J. Hu, Y. H. Lo, W. Y. Nie, T. Lee, J. Luo, K. S. Yang, K. I. Jang and S. Xu, Perovskite Superlattices with Efficient Carrier Dynamics, *Nature*, 2022, **608**, 317–323.

54 X. Li, Y. Zhang, Q. S. Liu, Z. H. Bai, L. L. Zhang and J. H. Zhang, Performance Study of $Ca_3Sc_2Si_3O_{12}$: Ce^{3+} Cyan-Green Fluorescent Converter for Laser lumination, *Ceram. Int.*, 2024, **50**, 25422–25433.

55 A. Halizati, S. Aierken and J. Y. He, Preparation of $BaAl_{2-x}Ga_xSi_2O_8$: Ce^{3+}, M^+ (Li, Na, K) Blue-Cyan Phosphors Based on Charge Compensation and Cation Substitution Strategies and Luminescence Performance Study, *Ceram. Int.*, 2024, **50**, 26077–26085.

56 G. Li, X. Lu, Q. Mao, G. Du, M. Liu, L. Chu and J. Zhong, Suppression of Charge Imbalance via Li^+-Mn^{4+} Co-Incorporated Sr_2YSbO_6 Red Phosphors for Warm WLEDs, *Mater. Today Chem.*, 2022, **23**, 100744.

57 Q. G. Huang, P. Sui, F. Huang, H. Lin, B. Wang, S. S. Lin, P. F. Wang, J. Xu, Y. Cheng and Y. S. Wang, Toward High-Quality Laser-Driven Lightings: Chromaticity-Tunable Phosphor-in-Glass Film with ''Phosphor Pattern'' Design, *Laser Photonics Rev.*, 2022, **16**, 2200040.

58 P. Liang, Z. Wu, Y. Y. Zhang, R. R. Hu, T. Q. Jia, Y. Yang, S. A. Zhang, Z. R. Sun and D. H. Feng, Electron Spin Dynamics in Ce^{3+}: YAG Crystals: Hyperfine Interaction of 4f and 5d Electrons, *Phys. Rev. B*, 2019, **99**, 024308.

59 G. Blasse and B. C. Grabmaier, *Luminescent Materials*, Springer, Berlin, 1994.

60 L. Q. Yao, Q. Y. Shao, X. X. Xu, Y. Dong, C. Liang, J. H. He and J. Q. Jiang, Broadband Emission of Single-Phase $Ca_3Sc_2Si_3O_{12}$: Cr^{3+}/Ln^{3+} (Ln = Nd, Yb, Ce) Phosphors for Novel Solid-State Light Sources with Visible to Near-Infrared Light Output, *Ceram. Int.*, 2019, **45**, 14249–14255.

61 D. J. Liu, G. G. Li, P. P. Dang, Q. Q. Zhang, Y. Wei, H. Z. Lian, M. M. Shang, C. C. Lin and J. Lin, Simultaneous Broadening and Enhancement of Cr^{3+} Photoluminescence in $LiIn_2SbO_6$ by Chemical Unit Cosubstitution: Night-Vision and Near-Infrared Spectroscopy Detection Applications, *Angew. Chem., Int. Ed.*, 2021, **60**, 14644–14649.

62 A. Lenef, J. F. Kelso, J. Serre, A. A. Kulkarni, D. Kinkenon and M. Avison, Co-Sintered Ceramic Converter for Transmissive Laser-Activated Remote Phosphor Conversion, *Appl. Phys. Lett.*, 2022, **120**, 021104.

63 H. Wang, Y. Mou, Y. Peng, Y. Zhang, A. G. Wang, L. L. Xu, H. L. Long, M. X. Chen, J. N. Dai and C. Q. Chen, Fabrication of Phosphor Glass Film on Aluminum Plate by Using Lead-Free Tellurite Glass for Laser-Driven White Lighting, *J. Alloys Compd.*, 2020, **814**, 152321.

64 J. Park, S. Cho and H. Kwon, Aluminum-Ceramic Composites for Thermal Management in Energy-Conversion Systems, *Sci. Rep.*, 2018, **8**, 17852.

65 S. S. Lin, H. Lin, Q. M. Huang, H. Y. Yang, B. Wang, P. F. Wang, P. Sui, J. Xu, Y. Cheng and Y. S. Wang, Highly Crystalline $Y_3Al_5O_{12}$: Ce^{3+} Phosphor-in-Glass Film: A New Composite Color Converter for Next-Generation High-Brightness Laser-Driven Lightings, *Laser Photonics Rev.*, 2022, **16**, 2200523.

66 P. Zheng, S. X. Li, T. Takeda, J. Xu, K. Takahashi, R. D. Tian, R. Wei, L. Wang, T. L. Zhou, N. Hirosaki and R. J. Xie, Unraveling the Luminescence Quenching of Phosphors under High-Power-Density Excitation, *Acta Mater.*, 2021, **209**, 116813.

67 P. Zheng, S. X. Li, L. Wang, T. L. Zhou, S. H. You, T. Takeda, N. Hirosaki and R. J. Xie, Unique Color Converter Architecture Enabling Phosphor-in-Glass (PiG) Films Suitable for High-Power and High-Luminance Laser-Driven White Lighting, *ACS Appl. Mater. Interfaces*, 2018, **10**, 14930–14940.